Journal of
Materials Chemistry A

Materials for energy and sustainability

Accepted Manuscript

This article can be cited before page numbers have been issued, to do this please use: H. Fattal, N. Spanier, A. Romem, S. Harpaz, J. Henderson, M. C. Biesinger, D. Mandler, N. Shpigel and D. Sharon, *J. Mater. Chem. A*, 2025, DOI: 10.1039/D5TA03206G.

ROYAL SOCIETY OF CHEMISTRY

rsc.li/materials-a

Anion-Guided Interphase Formation Stabilizes Reversible Iron Electrodeposition in Aqueous Electrolytes

Hadar Fattal[1], Netta Bruchiel Spanier[1*], Avigial Romem[1], Sara Harpaz[1], Jeffrey D. Henderson[2], Mark C. Biesinger[2,3], Daniel Mandler[1], Netanel Shpigel[4*], and Daniel Sharon[1*]

1. Institute of Chemistry, The Hebrew University of Jerusalem, 9190401, Jerusalem, Israel
2. Surface Science Western, The University of Western Ontario, London, N6G 0J3, ON, Canada
3. Department of Chemistry, The University of Western Ontario, London, N6A 5B7, ON, Canada
4. Department of Chemical Sciences, Ariel University, Ariel 40700, Israel.

Abstract

The reversible electrodeposition of iron metal in aqueous electrolytes is a promising strategy for enabling cost-effective, large-scale aqueous rechargeable batteries. However, its practical viability is hindered by parasitic side reactions, particularly the hydrogen evolution reaction (HER), which lowers Coulombic efficiency, and by the instability of deposited iron, leading to corrosion, capacity loss, and reduced cycle life. This study investigates the impact of three distinct ferrous-based electrolytes—sulfate ($FeSO_4$), chloride ($FeCl_2$), and trifluoromethane sulfonate ($Fe(OTf)_2$)—on the reversible deposition behavior and passivation dynamics of iron metal anodes. Surface analysis reveals that electrolyte composition critically influences passivation layer formation, directly affecting stability and efficiency. $FeSO_4$ and $Fe(OTf)_2$ generate compact, iron-oxide/hydroxide-rich films that suppress hydrogen evolution, resist corrosion, and deliver high Coulombic efficiencies during cycling. Notably, $Fe(OTf)_2$ is especially effective at stabilizing the electrodeposited iron metal during long-term storage, exhibiting minimal self-discharge behavior. Conversely, $FeCl_2$ leads to inadequate passivation, resulting in lower efficiency of electrodeposition and rapid loss of plated iron due to self-discharge. While increasing current density and electrolyte concentration can reduce water activity and improve deposition efficiency through kinetic regulation, we show that a stable, hydrated solid-electrolyte interphase is crucial for long-term corrosion protection and the durability of iron anodes in aqueous batteries.

View Article Online
DOI: 10.1039/D5TA03206G

Introduction

As the global demand for renewable energy solutions continues to rise, the development of advanced energy storage technologies that are both economically viable and environmentally sustainable becomes essential[1–4]. Among these technologies, aqueous batteries have been acknowledged for their potential in large-scale energy storage due to their high safety, low cost, high power density, and environmental friendliness.[5,6] These advantages have led to growing interest in aqueous batteries with metal anodes such as zinc, aluminum, and magnesium, which offer promising electrochemical properties and abundant availability, making them ideal for sustainable energy storage.[7–9] One of the most widely studied aqueous systems involves Zn metal anode, owing to its relatively low redox potential (−0.76 vs SHE) and abundant resource availability.[10,11] While having a more positive working potential (−0.44 vs SHE), iron metal anodes provide a slightly higher capacity (960 mAh/g versus zinc's 820 mAh/g) and are significantly more cost-effective.[12] This cost advantage is primarily because iron is orders of magnitude more abundant in Earth's crust compared to zinc (5.6% iron vs. 0.007% zinc), which makes it an exceptionally suitable candidate for large-scale energy storage applications.

The performance of iron-based batteries in aqueous environments is significantly affected by several key factors. In acidic electrolyte solutions, the hydrogen evolution reaction (HER) competes with iron deposition, as HER is thermodynamically more favorable under these conditions, often leading to inefficiencies in battery operation.[13–15] Furthermore, iron's inherent susceptibility to corrosion in aqueous environments accelerates the degradation of battery components, contributing to material loss and structural damage.[16] These challenges result in diminished Coulombic efficiency (CE) and a reduced operational lifespan of the iron-based battery.

To address these challenges, ongoing research has explored the integration of various additives into the iron anode formulation to enhance overall battery performance. The incorporation of citric and ascorbic acids into $FeCl_2$ electrolytes, for example, has been shown to improve iron deposition by forming complexes with metallic ions, resulting in smoother layers and enhanced cycling stability.[17,18] Additionally, employing high concentrations of electrolyte solutions has been shown to effectively reduce the HER rate. Hawthorne et al. demonstrated that increasing the concentration of chlorides in $FeCl_2$ with NaCl as a supporting electrolyte significantly improved the Coulombic efficiency.[19] Similarly, Liu et al. showed that iron metal anodes utilizing high concentrations of Mg or Ca-based electrolyte solutions exhibited markedly improved cycling stability, primarily due to suppressed water reduction.[20] Recent work by Greenburg et al. demonstrated that PEG[19]-water mixtures significantly improve Fe electrodeposition efficiency by reducing undesirable HER due to the high PEG concentration at the electrode interface.[21]

View Article Online
DOI: 10.1039/D5TA03206G

Despite these promising strategies, questions remain regarding the long-term cycling stability of active metals such as iron in water-containing electrolytes and the potential for self-discharge—both of which are critical for large-scale energy storage applications.[22] While the kinetic suppression of the hydrogen evolution reaction (HER) in either high-concentration solutions or water–organic mixtures effectively improves short-term plating efficiency, iron may still gradually react with water molecules, raising concerns about its durability over extended cycling.[23] Notably, findings from zinc-based aqueous batteries emphasize the critical role of electrolyte composition in governing the formation of electrode surface layers that sustain long-term cycling stability and mitigate self-discharge, suggesting that a similar influence may extend to iron-based systems.[24–28] Accordingly, this study seeks to clarify how variations in iron-based electrolyte solutions affect the stability and surface chemistry of electrodeposited iron, thereby impacting its efficiency and durability.

Herein, we examine the performance of iron electrodeposition and stripping on Cu foil using three distinct electrolytes: ferrous sulfate ($FeSO_4$), ferrous chloride ($FeCl_2$), and ferrous trifluoromethanesulfonate ($Fe(OTf)_2$). Utilizing a range of electrochemical and spectroscopic characterization techniques, we assess how each electrolyte influences the HER, corrosion behavior, and the overall efficiency and longevity of the electrodeposition process. We establish a definitive correlation between the choice of electrolyte and the formation of hydroxy/oxide passivation layers, pivotal for the stability and performance of reversible iron electrodeposition. Notably, our findings suggest that electrolytes based on $FeSO_4$ and $Fe(OTf)_2$ are particularly effective in promoting the formation of uniform passivation layers, thereby significantly enhancing the stability and durability of the cells.

Results and Discussion

To elucidate the impact of electrolyte composition on the reversible electrodeposition of iron, we investigated iron deposition and stripping in half-cell configurations using 1 M solutions of $FeSO_4$, $FeCl_2$, or $Fe(OTf)_2$. Galvanostatic charge-discharge (GCD) measurements were conducted within asymmetric cells utilizing copper foil as the working electrode, iron as the counter electrode, and glass fiber as the separator. Given the variability in individual cell performance, we rigorously validated our findings. Each electrolyte system underwent testing with at least three identical cells. The data presented here reflect the averaged cycle life values from these tests.

View Article Online
DOI: 10.1039/D5TA03206G

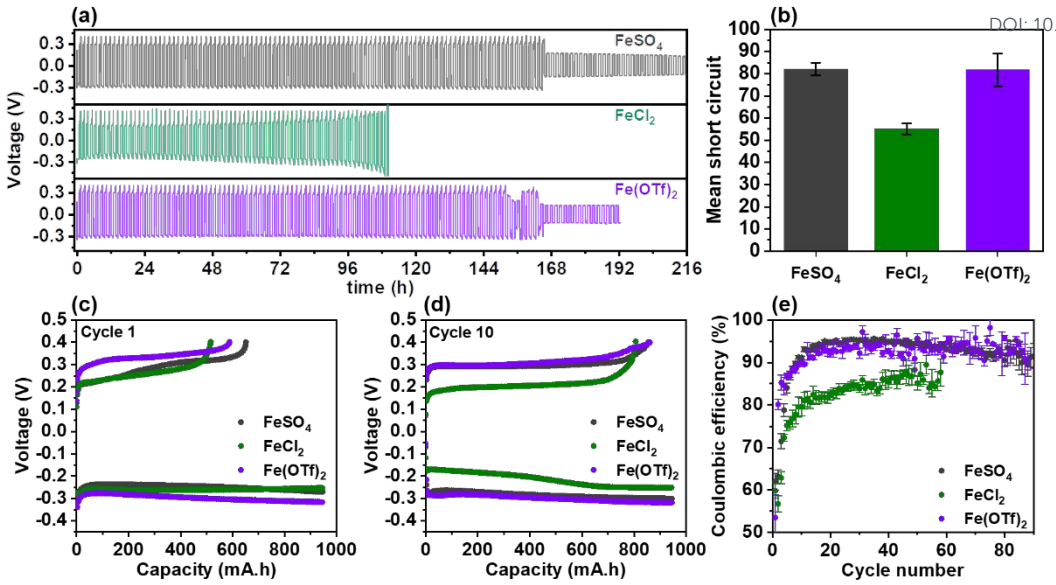

Figure 1. *(a) Voltage profiles of long-term Fe metal deposition/stripping cycling containing different electrolytes in a Cu||Fe cell at 1 mA/cm² for 50 min.(b) Comparison of the average cycle number prior to short circuit for different electrolytes. The deposition/stripping voltage profile of (c) the 1st and (d) the 10th cycle. (e) The average Coulombic efficiency of Fe deposition/stripping with different electrolytes.*

The voltage profiles over time, shown in **Figure 1a**, highlight significant differences in the cycling durability of cells with the three different electrolyte systems. The $FeCl_2$ electrolyte shows a more rapid decline in stability, leading to short circuits after approximately 55 ± 3 cycles (**Figure 1b**). In contrast, the $FeSO_4$ and $Fe(OTf)_2$ electrolytes demonstrate much more stable voltage profiles throughout the extended cycling period, maintaining performance for about 80 ± 8 cycles before exhibiting signs of voltage fluctuation, which may indicate the formation of soft short circuits. Similar trends were observed in symmetric Fe‖Fe cells (**Figure S1**), where $FeSO_4$- and $Fe(OTf)_2$-based electrolytes demonstrated superior average cycle life at both 1 and 2.5 mA cm^{-2} compared to $FeCl_2$, further supporting their enhanced cycling stability.

Figures 1c and **1d** present the voltage profiles for the first and tenth cycles of iron electrodeposition using the three electrolyte solutions. In the first cycle, all three electrolytes exhibit stable voltage plateaus between −0.2 and −0.3 V vs. Fe/Fe^{2+} during reduction, which can be associated with the Fe electrodeposition accompanied by an overpotential. The $Fe(OTf)_2$ electrolyte shows slightly higher overpotentials compared to $FeSO_4$ and $FeCl_2$. A large hysteresis is observed between the deposition and stripping processes for all electrolyte solutions, with $Fe(OTf)_2$ displaying the largest difference between the reduction and oxidation plateaus. By the tenth cycle, the electrodeposition overpotential for $FeCl_2$ has significantly decreased. The profile of $Fe(OTf)_2$ remains stable throughout cycling, while $FeSO_4$ shows a slight increase in

View Article Online
DOI: 10.1039/D5TA03206G

overpotential, with both profiles ultimately exhibiting similar behavior at the tenth cycle, with higher overpotentials during deposition and stripping processes compared to $FeCl_2$. Additionally, by the tenth cycle, a significant difference in efficiency is evident, as indicated by the longer stripping process for $FeSO_4$- and $Fe(OTf)_2$-based cells.

The reduced overpotential in $FeCl_2$ may indicate that the deposited iron developed a more extensive surface area, possibly becoming more porous or rougher over time. This increased surface area would lower the effective current density, thereby reducing the overpotential. In contrast, the more consistent voltage response observed for $FeSO_4$ and $Fe(OTf)_2$ implies that no significant changes in the deposition process occurred with cycling. The larger overpotential associated with these electrolytes suggests higher resistance within the deposited layer, requiring a higher potential to drive both deposition and dissolution during stripping. The higher resistance observed in $FeSO_4$ and $Fe(OTf)_2$-based cells potentially suggests the formation of a passivation layer during the electrodeposition process, which may contribute to their enhanced stability compared to $FeCl_2$. To further assess the robustness of these systems under more demanding conditions, additional cycling experiments were performed at 70 °C (Figure S3). As expected, all electrolyte systems showed accelerated degradation at elevated temperature, however, the trend of enhanced stability in $FeSO_4$ and $Fe(OTf)_2$ relative to $FeCl_2$ was preserved.

The average coulombic efficiency (CE) during cycling for the three electrolyte systems is depicted in **Figure 1e**. Initially, all three electrolytes exhibit an increase in CE as the deposition and stripping processes stabilize, a trend that can be ascribed to the stabilization of surface films on the Cu substrate. After this stabilization period, $FeSO_4$ and $Fe(OTf)_2$ consistently exhibit substantially higher CE compared to $FeCl_2$. Specifically, both $FeSO_4$ and $Fe(OTf)_2$ achieve a CE of up to 95 ± 5% after 15 cycles, maintaining this high efficiency throughout the subsequent cycles until cell failure. In contrast, $FeCl_2$ reaches a maximum CE of only 85 ± 2% after 30-40 cycles, indicating a less efficient performance over time.

View Article Online
DOI: 10.1039/D5TA03206G

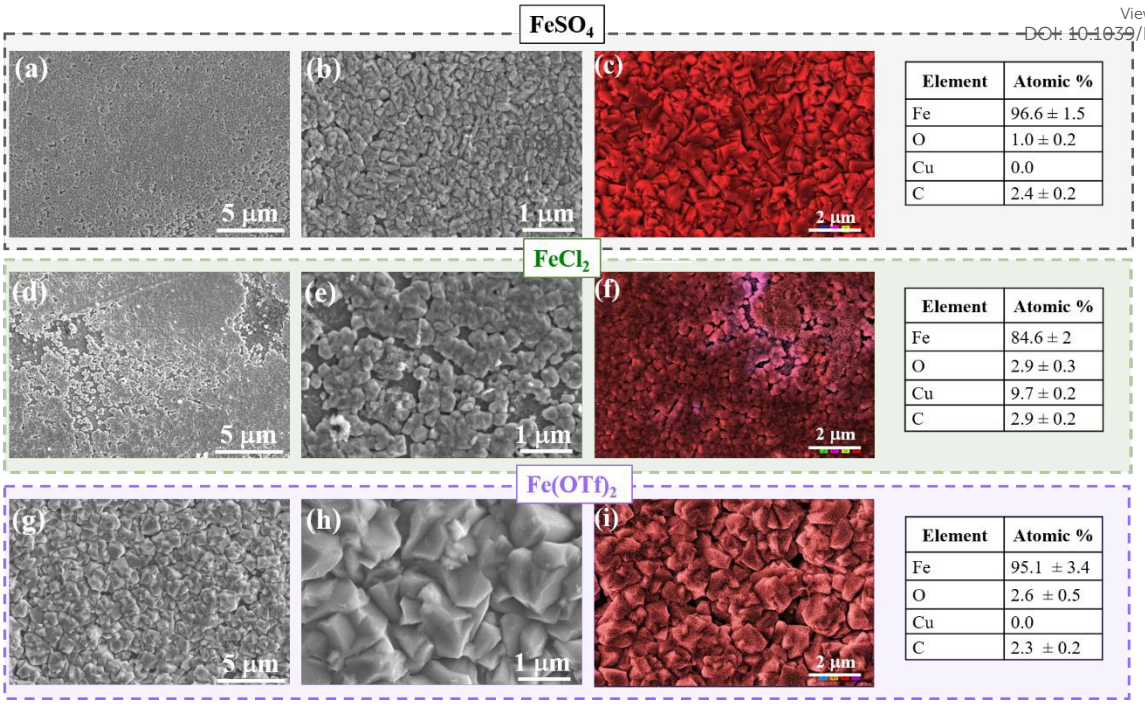

Figure 2. *SEM images and EDS analysis (c, f and i) obtained after the first deposition of Fe on Cu foil in cells containing 1M (a-c) $FeSO_4$, (d-f) $FeCl_2$ and (g-i) $Fe(OTf)_2$ electrolyte solutuions.*

Following the electrochemical analysis, the morphology of the iron deposits, collected from cells after the first electrodeposition process, was examined using scanning electron microscopy (SEM), as shown in **Figure 2(a-h)**. The morphology varied significantly with electrolyte composition. In $Fe(OTf)_2$-based cells, iron formed large, faceted crystals arranged in a compact and uniform layer. $FeSO_4$ produced smaller but densely packed grains that also provided complete substrate coverage. In contrast, $FeCl_2$ resulted in a rough and irregular deposit composed of small, dispersed particles with visible voids and exposed copper, indicating poor coverage. These differences suggest variations in nucleation and growth kinetics between the electrolytes. While crystal size alone does not correlate directly with electrochemical performance, as both $FeSO_4$ and $FeCl_2$ produce small grains but differ markedly in stability, the non-uniformity and incomplete coverage in $FeCl_2$ deposits likely contribute to its reduced cycling performance. Such morphological inhomogeneities may arise from less controlled deposition dynamics or enhanced corrosion, both of which can promote early short-circuiting and capacity loss.[29–31] Energy-dispersive X-ray spectroscopy (EDS) supports these observations, showing that the deposits from $FeCl_2$ have an atomic iron percentage of only 84.6 ± 2 %, with a visible copper presence of 9.7 ± 0.2 % (**Figures 2c**). EDS mapping for $FeSO_4$ and $Fe(OTf)_2$ indicates that these layers are predominantly iron, with atomic percentages of 96.6 ± 1.5% and 95.1 ± 3.4% respectively, and no detectable copper, indicating complete substrate coverage (**Figure 2f** and **h**). The uniform coverage achieved with sulfate and triflate-based electrolyte solutions may correlate with enhanced cycling stability and efficiency in these cells.

View Article Online
DOI: 10.1039/D5TA03206G

To further assess the composition of the deposited crystals, we analyzed the X-ray diffraction (XRD) patterns of electrodes obtained after the first electrodeposition process from cells containing different electrolyte solutions. As seen in **Figure 3a** the patterns reveal distinct peaks at angles of 45°, 65° and 82°, corresponding to the (110), (200) and (211) crystal planes, respectively, confirming the successful deposition of crystalline iron from all tested electrolytes. Notably, the XRD analysis shows no evidence of crystalline side products, which are typically observed during the deposition of metals such as Zn, Mg, and Al in aqueous solutions.[32–34] For instance, the deposition of Zn from analogous salts in mildly acidic conditions often leads to the formation of crystalline hydroxy sulfates and chlorides. In zinc metal formation, such side products are believed to compromise the efficiency of reversible deposition[27,28,35]. However, this issue does not appear to affect iron metal deposition, suggesting that different mechanisms govern the performance of iron deposition. Additionally, the consistent absence of side products, even after ten deposition cycles (**Figure S3**), confirms that the formation of such side products does not occur with continuous cycling.

To elucidate the surface chemistry of iron deposits, we analyzed the Fe $2p_{3/2}$ and O 1s XPS spectra from iron electrodeposited on Cu foil using three different electrolytes (**Figure 3c and d**). The Fe $2p_{3/2}$ spectra from films deposited from $FeCl_2$-based electrolytes exhibit a significant peak for metallic iron at 706.9 eV. At higher binding energies, a broad peak corresponding to iron compounds with higher oxidation states of Fe^{+2} and Fe^{+3} is observed. Previously reported fitting parameters were used to deconvolute the complex multiple-splitting structure of these compounds.[36,37] The results indicate the presence of oxide species such as Fe_2O_3 and Fe_3O_4, constituting approximately 17 and 43% of the total iron signal, respectively. Considering XPS's penetration depth of a few nanometres (7-10 nm), the substantial presence of a metallic iron signal, constituting approximately 30% of the total iron signal, indicates that the oxide layers are very thin and potentially non-uniform across the iron surface. Using oxide thickness calculations[38,39] modified with a weighted average oxide scheme[40,41] and using the above oxide percentages gave an average mixed oxide thickness of 2.1 nm. This observation aligns well with previous findings by Nagayama and Cohen, who noted that passivated iron is typically covered with a thin film of Fe_2O_3 and Fe_3O_4, ranging in thickness from 1–3 nm.[42]

The Fe $2p_{3/2}$ XPS spectra from the sulfate-based electrolyte reveal the presence of metallic iron at approximately 706.7 eV, alongside a broad peak indicative of Fe^{+2} and Fe^{+3} oxidation states. Deconvolution of this peak identifies oxy-hydroxide FeOOH as the most prevalent species within the passivation layer, contributing approximately 40 % of the total signal. Additionally, Fe_3O_4 and Fe_2O_3 account for approximately 29 and 20% of the total signal, respectively. Notably, the intensity of the metallic iron peak is diminished compared to that observed in samples from the

View Article Online
DOI: 10.1039/D5TA03206G

chloride-based electrolyte, suggesting the formation of a thicker (calculated to be 4.8 nm) and more homogeneous passivation layer under sulfate conditions. This reduction in metallic iron signal intensity is even more pronounced in samples from the triflate-based electrolyte, where the metallic iron peak is substantially reduced, indicating extensive coverage by oxidized species (~8 nm). Moreover, the content of oxy-hydroxide FeOOH is notably higher relative to oxide species, underscoring its significant role in passivation.[43–46] The formation of these oxide and oxy-hydroxide layers in the presence of sulfate, and more so with triflate, suggests they effectively act as protective barriers on the iron metal surface, enhancing corrosion resistance.

Further insights into the oxide and hydroxide species present on the iron surface are gleaned from oxygen XPS spectra analysis. Two principal O 1s peaks are consistently observed across all samples: one at 529.9 eV indicative of lattice oxides and another at approximately 531.5 eV, representing hydroxides and/or defect oxides. Notably, the relative intensities of the lattice and defect/hydroxide peaks vary significantly among the samples, highlighting differences in surface chemistry. In the chloride-based samples, the oxide peak is more pronounced, suggesting a predominance of iron oxides with a relatively lower hydration state on the surface. This is consistent with the deconvolution of the Fe $2p_{3/2}$ spectra.

As we transition to the sulfate-based samples, the intensity of the peaks corresponding to hydroxides in the O 1s spectra becomes more pronounced, indicating a shift towards more hydrated species. In the triflate-based samples, the hydroxide peak surpasses the oxide peak in intensity, signaling a substantially higher degree of hydration within the passivation layer. This observation aligns with the deconvolution of the Fe $2p_{3/2}$ spectra which suggests greater amounts of FeOOH on the sulfate and triflate-based sample surfaces. This increasing hydroxide content correlates with the formation of thicker and more uniform passivation layers, enhancing the protective properties of the barrier layer against corrosion. Additional components for organic, sulfate, and triflate species were included where appropriate in the O 1s spectra. Their presence is supported by peaks observed in the S 2p and F 1s XPS spectra, as detailed in the supporting information (**Figure S4**). While there is significant overlap between sulfate, triflate, defect oxides, hydroxides, and organic oxygen species originating from adventitious carbon, the relative size of the triflate, sulfate, and organic components was guided by stoichiometry (details reported elsewhere).[47,48] These species may also contribute to the robustness of the passivation layer, further enhancing corrosion resistance and cell cycling stability.[49]

View Article Online
DOI: 10.1039/D5TA03206G

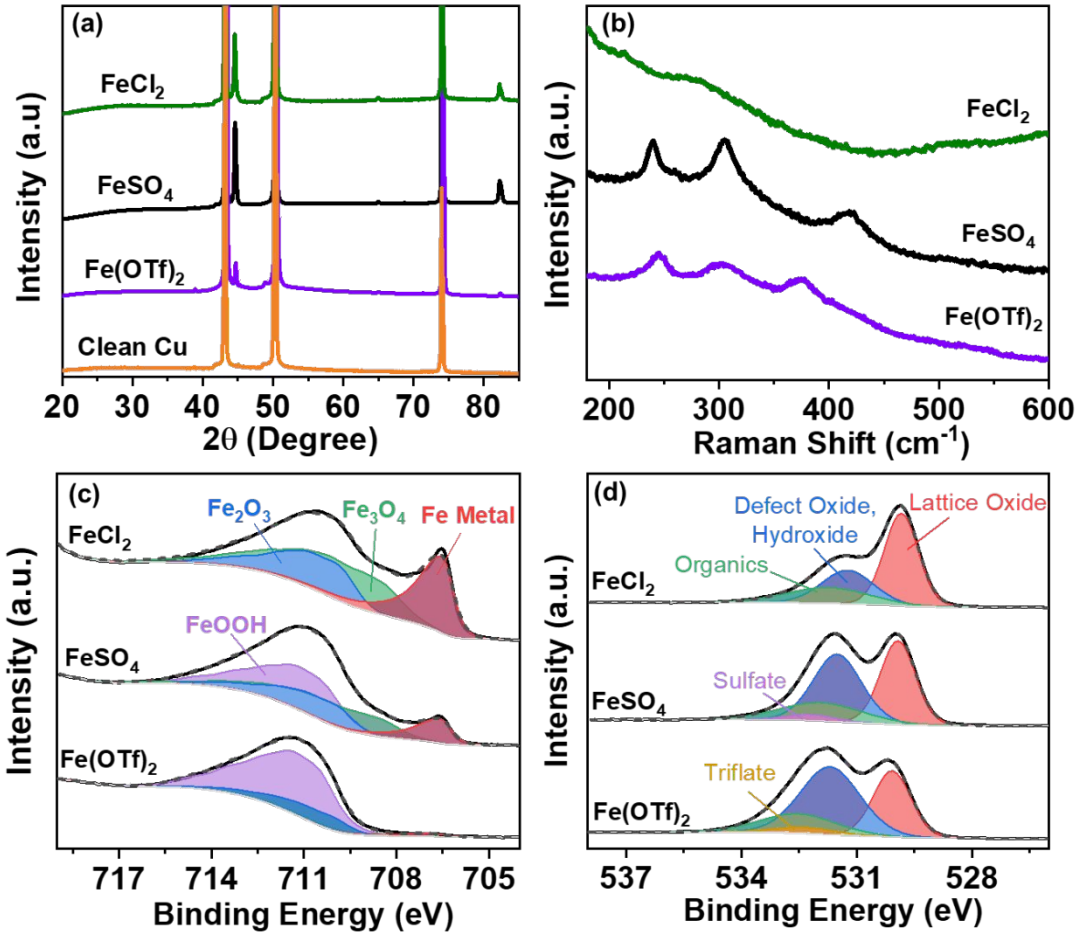

Figure 3. *(a) XRD patterns after the first deposition of Fe on Cu foil at 1 mA/cm² for 50 min Raman (b) and XPS of Fe $2p_{3/2}$ (c) and O 1s (d) and spectra after the first deposition of Fe on Cu electrode from different aqueous electrolyte solutions. Please note that the XPS spectra were charge-corrected according to adventitious carbon (284.8 eV).* [50,51] V. The corresponding C 1s spectra for each electrolyte system are provided in the Supporting Information (Figure S4).

Raman spectroscopy was employed to provide additional insights into the specific species present on the electroplated iron surface. **Figure 3b** displays the Raman spectra of Fe metal electrodeposited on Cu foil from the three examined electrolyte solutions. Characteristic peaks corresponding to iron-based oxide and hydroxide compounds are identified for the iron deposited from the sulfate and triflate electrolyte solutions. Both samples exhibit a peak in the range of 240–244 cm^{-1} and a second peak in the range of 303–305 cm^{-1}, which can be attributed to FeOOH.[52,53] Additional peaks, observed at ≈ 374 cm^{-1} for the triflate solution and at ≈ 415 cm^{-1} for the sulfate-based sample, can be attributed to Fe_2O_3, Fe_3O_4, as well as different phases of FeOOH.[54,55]

In contrast to the sharp and well-defined Raman spectra of the sulfate- and triflate-based samples, the Raman spectrum of the iron deposited from the chloride-based solution lacks significant peaks

associated with oxidized species, indicating a much lower content of oxidized surface species. We note that while Raman measurements do not clearly reveal oxide species in the $FeCl_2$ sample, XPS detects the presence of Fe_2O_3 and Fe_3O_4. This difference may arise from the lower sensitivity of Raman spectroscopy to thin or non-uniform surface layers, especially when the oxide content is low and the signal is further suppressed by the underlying metallic iron. Although the absence of Raman peaks does not definitively rule out the presence of iron oxides, it may reflect the limited extent and lower quality of the passivation layer formed in the chloride-based electrolyte. This interpretation is consistent with the overall spectroscopic trends observed across all samples, though we acknowledge it cannot be confirmed solely from the Raman measurements. Nevertheless, the Raman spectra from the sulfate- and triflate-based samples clearly confirm the presence of FeOOH as a dominant component in the passivation layer.

While the formation of hydroxy-based species in aqueous Zn-based systems often leads to increased resistance and degraded performance, the decomposition of aqueous electrolyte solutions in Fe-based systems can instead result in beneficial interfacial layers. Corrosion studies suggest that the dense aggregation of rust particles can effectively passivate metal surfaces against further corrosion by forming cohesive and tightly adherent films.[44] Specifically, for iron, this protective mechanism is effectively achieved through layers of both crystalline and amorphous oxyhydroxide (FeOOH) species, which are known for their superior corrosion resistance.[43–46] Consequently, the presence of thicker and richer FeOOH layers in samples utilizing sulfate and triflate-based electrolytes likely contributes to their enhanced cycling performance, as compared to those using chloride-based solutions.

To gain insights into the formation of the passivation layers during the electrodeposition process we employed Electrochemical Impedance Spectroscopy (EIS). The Nyquist plots shown in **Figure 4** illustrate the impedance behavior of iron electrodeposited from the three different electrolytes after 1, 10, and 30 cycles. After the first deposition processes, each system exhibited a single semicircle in the Nyquist plots, indicative of charge transfer resistance (Rct) at the metal/electrolyte interface, a marker of initial passivation effectiveness.[56,57] Notably, the $FeCl_2$-based samples exhibited the smallest semicircle, indicating the lowest charge transfer resistance and suggesting a less effective initial passivation layer. In stark contrast, samples containing $FeSO_4$ and $Fe(OTf)_2$ electrolytes displayed progressively larger semicircles, denoting increased resistance to charge transfer. This behavior supports the formation of more robust passivation layers that likely contribute to enhanced stability and durability of the electrodeposited iron, mitigating early degradation and improving overall electrochemical performance.

As the electrodeposition progresses to the tenth cycle, distinct behaviors emerge among the electrolytes (**Figure 4b**). In the case of $FeCl_2$, the semicircle observed in the Nyquist plot

View Article Online
DOI: 10.1039/D5TA03206G

decreases in size, indicative of reduced charge transfer resistance. This reduction in charge transfer resistance, which aligns well with the decreased voltage hysteresis shown in **Figure 1d**, suggests the facilitation of more rapid electrochemical reactions at the metal/electrolyte interface in the $FeCl_2$ system. This behavior may originate from poor interfacial stability of the Fe in the presence of Cl^-, making it more susceptible to corrosion reactions upon cycles. Conversely, the $FeSO_4$ and $Fe(OTf)_2$ systems exhibit an increase in the size of their capacitive semicircles, suggesting the formation of increasingly effective passivation layers. A high-frequency semicircle is observed by the tenth cycle, becoming more pronounced by the thirtieth (**Figure 4c, inset**), indicating the development of a stable passivation layer at the iron-electrolyte interface

In EIS spectrum of passivated/coated metals, when more than one semicircle is observed, the low-frequency semicircle typically reflects charge transfer resistance (R_{ct}) processes related to corrosion reactions at the metal-electrolyte interface, as previously discussed.[56] We note that the response attributed to R_{ct} may also be affected by variations in the true surface area of the electrodeposited iron. Differences in morphology, roughness, and non-uniformity, as observed in the SEM images (Figure 2), could contribute to the apparent R_{ct} values measured across the different electrolyte systems. Furthermore, enhanced corrosion, as suspected in the $FeCl_2$ system, may further increase the surface area of the deposit over time, which could manifest as a reduced charge transfer resistance. Nonetheless, the overall increase R_{ct} for $FeSO_4$ and $Fe(OTf)_2$ compared to $FeCl_2$, together with the emergence of a distinct high frequency semicircle attributed to passivation layer resistance, aligns with the formation of more stable interphases. This interpretation is further supported by Raman and XPS analyses, confirming the development of protective layers that suppress side reactions and enhance cycling stability.

To evaluate the long-term stability and corrosion resistance of electrodeposited iron, a standing corrosion test was conducted. This test quantifies the self-discharge behavior of the plated iron in various electrolyte solutions, providing insights into the effectiveness of the passivation layers in mitigating corrosion. As depicted in **Figure 4d**, the protocol begins with 20 stabilization cycles to ensure consistent iron deposition onto the substrate. After this initial phase, the cell undergoes a series of rest periods at specified intervals. Following each interval, the remaining iron is stripped (Q_2) and compared to the iron stripped after the initial stabilization (Q_1) to determine the capacity retention during storage. The test sequence concludes with 5 additional stabilization cycles before introducing a longer rest period.

Figure 4e displays the capacity retention of electrodeposited iron from three different electrolytes—$FeCl_2$, $FeSO_4$, and $Fe(OTf)_2$—over rest periods of 12, 24, and 48 hours. $FeCl_2$-based cells exhibit the highest self-discharge among the tested electrolytes. After 12 hours, capacity retention drops to 80.5 ± 2 %, decreases to 75 ± 4 % at 24 hours, and further declines to

View Article Online
DOI: 10.1039/D5TA03206G

60 ± 6 % by 48 hours. The observed decrease in capacity retention with longer rest periods is expected, as the plated iron is exposed to the solution for longer durations, leading to greater corrosion. Notably, $FeCl_2$ cells exhibit a particularly pronounced initial drop, losing nearly 20 % of the plated iron within the first 12 hours. Following this sharp decline, the degradation rate slows but remains significant, displaying a more linear decrease over the subsequent hours.

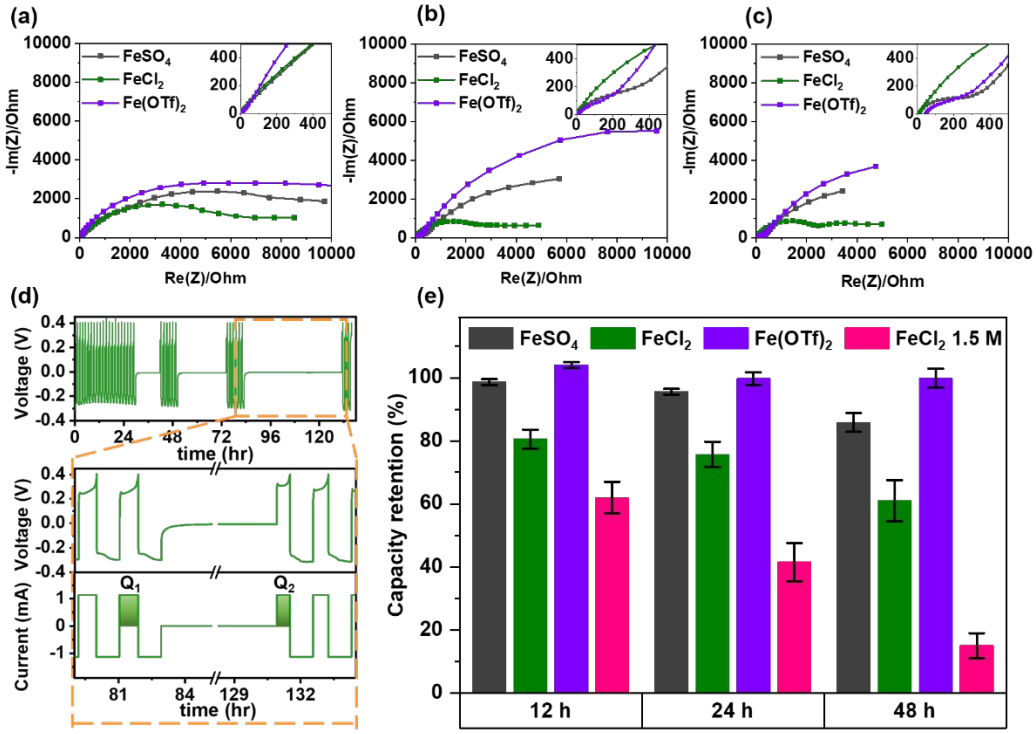

Figure 4. *Nyquist plots for Cu||Fe cell with different electrolyte solutions after 1 (a), 10 (b) and 30 Fe deposition cycles (d) The voltage profiles of Fe metal deposition/stripping cycling containing 1 M $FeCl_2$ followed a rest prior to stripping. (e) standing corrosion test for different electrolytes.*

In contrast, $FeSO_4$-based cells demonstrate much more moderate changes in capacity retention over time. With retentions of 98.6±1%, 95±1%, and 86±3% after the respective durations, these results suggest that the iron deposits from $FeSO_4$ are more stable and less prone to spontaneous self-discharge. Furthermore, the $FeSO_4$-based cells show a consistent linear decline, which is smaller than that of $FeCl_2$, with no initial large capacity loss. This substantially lower corrosion rate can be attributed to the formation of a protective oxy-hydroxide layer that inhibits further iron dissolution.

Cells containing $Fe(OTf)_2$ exhibit the highest corrosion resistance, with almost no loss of charge observed after all rest periods. This behavior further supports the formation of a dense and thick protective layer on the iron surface, consistent with the homogeneous passivation layer observed in XPS analysis. This robust layer effectively shields the underlying iron from corrosion while

still permitting ion transfer between the electrolyte and the deposition sites as can be seen from its cycling behavior. These findings highlight the high corrosion resistance of the protective layers formed in $FeSO_4$ and $Fe(OTf)_2$ electrolytes, with the denser and more uniform layer in $Fe(OTf)_2$ providing the greatest long-term stability during extended rest periods.

The differences in passivation effectiveness among triflate, sulfate, and chloride ions can be attributed to differences in the solubility of iron species (both Fe^{2+} and Fe^{3+}). Chloride ions, which form the most soluble complexes with iron, lead to a higher dissolution rate of the passive film, thereby reducing its stability.[58,59] It has been proposed that chlorides specifically dissolve the outer iron oxide (Fe_2O_3) layer on iron-based layers, corroborating our spectroscopic findings.[60] In contrast, triflate ions form less soluble iron complexes, promoting a more stable and pronounced passivation layer, while sulfate ions exhibit intermediate solubility behavior. Additionally, the interaction of these anions with the iron matrix during passive film formation significantly alters its thickness, composition, and microstructure—key factors in determining the stability of the passive layer. Chloride anions, known for actively disrupting passivation processes, compete with hydroxide ions for binding sites on the metal surface, enhancing corrosion by disrupting the iron surface passivity.[29,61,62] Conversely, triflate and sulfate anions contribute to the formation of a substantial oxide layer, indicating less interference in the buildup and suggesting a less aggressive impact on the iron surface.

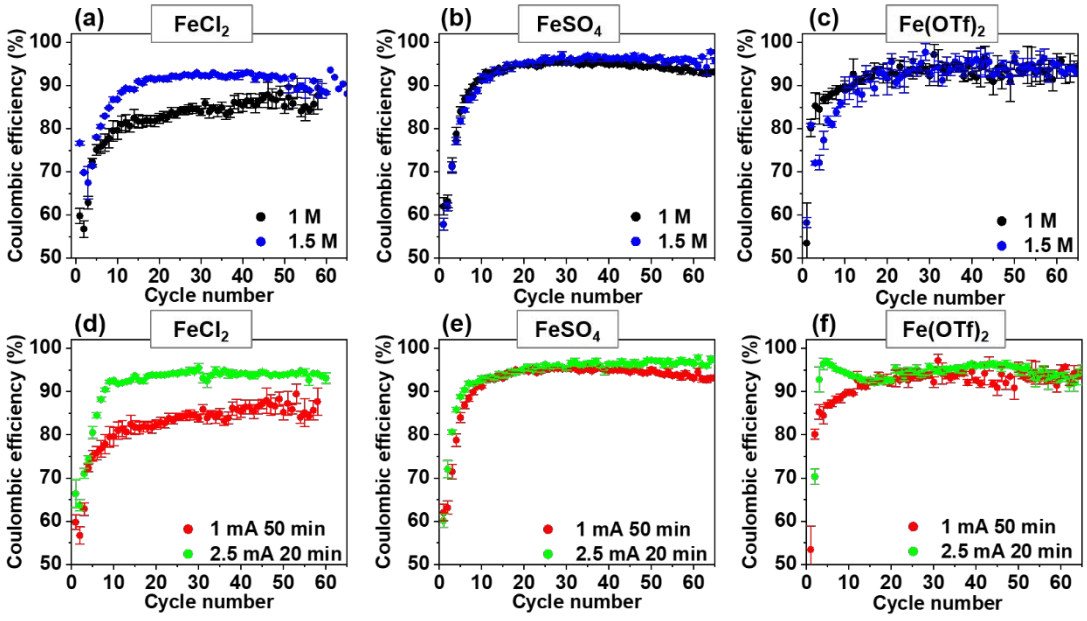

Figure 5. *The average CE Values of Fe deposition/stripping on Cu in various electrolytes at different concentrations (a-c) and currents (d-f)*

Given that the hydrogen evolution reaction (HER) competes with iron deposition, it has been proposed that increasing both electrolyte concentration and current density can improve coulombic efficiency (CE) by suppressing these undesired reactions.[20] These strategies have been

View Article Online
DOI: 10.1039/D5TA03206G

widely demonstrated in aqueous zinc-metal systems, where higher concentrations of chloride salts effectively reduce HER activity.[63,64] Moreover, it has been shown that higher deposition current densities lead to improved CE by preferentially favoring iron deposition due to its relatively faster kinetics compared to HER.[35,65] **Figure 5** illustrates the average CE of various iron-based electrolyte solutions under different current densities and electrolyte concentration conditions.For $FeCl_2$-based cells, CE increases with higher current densities, reaching 94% ± 1% at 2.5 mA/cm² in 1 M solutions (**Figure 5d**). This improvement is attributed to the accelerated iron deposition process at higher current densities, which further outpaces the slower kinetics of hydrogen evolution reactions (HER), thereby enhancing deposition efficiency. Additionally, increasing the $FeCl_2$ concentration to 1.5 M (**Figure 5a**) further improved CE to 92% ± 1%. The higher salt concentration likely reduces water activity in the electrolyte, thereby minimizing competing reactions with water.

In contrast, the $FeSO_4$ and $Fe(OTf)_2$ systems do not exhibit significant changes in CE with increased concentration or current density, maintaining a stable efficiency of approximately 96% (**Figure 5**). This lack of variation may be attributed to the formation of stable passivation layers, which effectively suppress contact between the deposited iron and water, thereby minimizing the influence of HER. However, despite the high and consistent CE, some inefficiencies remain. These are likely due to the consumption of iron during the formation of the passivation layers or the production of disconnected iron particles during plating, which do not contribute to the overall deposition process. Further investigation is needed to fully understand these mechanisms and their contributions to the observed efficiency limitations.

While the $FeCl_2$ system shows improved efficiency with higher concentration and current density, this does not translate to enhanced overall stability. Increasing the $FeCl_2$ concentration to 1.5 M exacerbates the self-discharge rate, with capacity retention dropping to 41±5% after 24 hours, compared to 75±4% with 1 M $FeCl_2$ (**Figure 4e**). This demonstrates that while higher concentrations improve cycling efficiency by suppressing side reactions during deposition, they fail to mitigate the underlying thermodynamic instability that drives self-discharge. The absence of effective passivation in $FeCl_2$-based cells leaves the plated iron highly susceptible to continuous dissolution. Additionally, the well-documented role of higher chloride concentrations in accelerating metal corrosion further compounds the instability of these systems, emphasizing the challenges of achieving long-term stability in a $FeCl_2$ electrolyte.

These findings underscore the critical importance of balancing both kinetic and thermodynamic stability in aqueous battery systems. Our study demonstrates that real passivation of metal anodes in aqueous solutions can be achieved, forming a solid-electrolyte interphase (SEI) that suppresses electron transport between the electrode and the electrolyte while enabling efficient ionic

View Article Online
DOI: 10.1039/D5TA03206G

transport. This unique property allows electrochemical reactions to proceed efficiently while protecting the underlying metal from dissolution. While kinetic enhancements, such as increased current density and electrolyte concentration, can temporarily improve efficiency by suppressing side reactions, they fail to address the fundamental thermodynamic challenges necessary for long-term stability. Building on this foundation, broader investigations into electrolyte selection, including diverse iron salt chemistries, may reveal further opportunities to enhance the stability and reversibility of aqueous iron-based systems.

Conclusions

This study highlights the critical role of electrolyte composition and operating conditions in determining the performance and stability of iron metal anodes in aqueous rechargeable batteries. Our findings demonstrate that the choice of electrolyte significantly influences the formation of the passivation layer on the electrodeposited iron surface, which in turn impacts the anode's efficiency, reversibility, and durability.

$FeCl_2$-based cells fail to form substantial passivation layers, leaving the plated iron highly exposed to the electrolyte. This increased exposure enhances susceptibility to hydrogen evolution reactions (HER) and accelerates corrosion. Together, these factors reduce Coulombic efficiency (CE) and severely limit the long-term stability of the cell, rendering $FeCl_2$ less suitable for applications requiring durability and reliable cycling performance.

Cells containing $FeSO_4$ and $Fe(OTf)_2$ solutions demonstrate significant advantages over $FeCl_2$, as they promote the formation of stable and uniform passivation layers that significantly enhance CE and improve the long-term cycling stability of iron deposits. These electrolytes exhibit superior resistance to corrosion and substantially improved self-discharge behavior, effectively addressing two critical challenges in aqueous systems. Notably, $Fe(OTf)_2$ stands out for its ability to form a complete and dense passivation layer on the iron metal surface, effectively inhibiting corrosion of the deposit even after 48 hours. These findings highlight the critical role of a hydrated solid-electrolyte interphase (SEI) in enabling truly rechargeable and stable aqueous metal-based batteries. Optimizing the protective properties of such passivation layers could potentially lead to the Coulombic efficiencies required for long-term cycling stability in battery applications.

References

(1) Olabi, A. G.; Abbas, Q.; Shinde, P. A.; Abdelkareem, M. A. Rechargeable Batteries: Technological Advancement, Challenges, Current and Emerging Applications. *Energy* **2023**, *266*, 126408. https://doi.org/10.1016/J.ENERGY.2022.126408.

(2) Ahmad, T.; Zhang, D. A Critical Review of Comparative Global Historical Energy Consumption and Future Demand: The Story Told so Far. *Energy Reports* **2020**, *6*, 1973–1991. https://doi.org/10.1016/J.EGYR.2020.07.020.

(3) Madlener, R.; Specht, J. M.; Hester, R. E.; Harrison, R. M. Business Opportunities and the Regulatory Framework. *Issues in Environmental Science and Technology* **2018**, *2019-January* (46), 296–326. https://doi.org/10.1039/9781788015530-00296.

(4) Comello, S.; Reichelstein, S. The Emergence of Cost Effective Battery Storage. *Nature Communications 2019 10:1* **2019**, *10* (1), 1–9. https://doi.org/10.1038/s41467-019-09988-z.

(5) Chao, D.; Zhou, W.; Xie, F.; Ye, C.; Li, H.; Jaroniec, M.; Qiao, S. Z. Roadmap for Advanced Aqueous Batteries: From Design of Materials to Applications. *Sci Adv* **2020**, *6* (21). https://doi.org/10.1126/SCIADV.ABA4098.

(6) Liang, Y.; Yao, Y. Designing Modern Aqueous Batteries. *Nature Reviews Materials 2022 8:2* **2022**, *8* (2), 109–122. https://doi.org/10.1038/s41578-022-00511-3.

(7) Zhang, X.; Lv, R.; Tang, W.; Li, G.; Wang, A.; Dong, A.; Liu, X.; Luo, J.; Zhang, X.; Lv, R.; Tang, W.; Li, G.; Wang, A.; Liu, X.; Luo, J.; Dong, A. Challenges and Opportunities for Multivalent Metal Anodes in Rechargeable Batteries. *Adv Funct Mater* **2020**, *30* (45), 2004187. https://doi.org/10.1002/ADFM.202004187.

(8) Yan, C.; Lv, C.; Jia, B. E.; Zhong, L.; Cao, X.; Guo, X.; Liu, H.; Xu, W.; Liu, D.; Yang, L.; Liu, J.; Hng, H. H.; Chen, W.; Song, L.; Li, S.; Liu, Z.; Yan, Q.; Yu, G. Reversible Al Metal Anodes Enabled by Amorphization for Aqueous Aluminum Batteries. *J Am Chem Soc* **2022**, *144* (25), 11444–11455. https://doi.org/10.1021/JACS.2C04820.

(9) Wang, H.; Tan, R.; Yang, Z.; Feng, Y.; Duan, X.; Ma, J. Stabilization Perspective on Metal Anodes for Aqueous Batteries. *Adv Energy Mater* **2021**, *11* (2), 2000962. https://doi.org/10.1002/AENM.202000962.

(10) Lu, W.; Zhang, C.; Zhang, H.; Li, X. Anode for Zinc-Based Batteries: Challenges, Strategies, and Prospects. *ACS Energy Lett* **2021**, *6* (8), 2765–2785. https://doi.org/10.1021/ACSENERGYLETT.1C00939.

(11) Kang, L.; Cui, M.; Zhang, Z.; Jiang, F. Rechargeable Aqueous Zinc-Ion Batteries with Mild Electrolytes: A Comprehensive Review. *Batter Supercaps* **2020**, *3* (10), 966–1005. https://doi.org/10.1002/BATT.202000060.

(12) He, Z.; Xiong, F.; Tan, S.; Yao, X.; Zhang, C.; An, Q. Iron Metal Anode for Aqueous Rechargeable Batteries. *Mater Today Adv* **2021**, *11*, 100156. https://doi.org/10.1016/J.MTADV.2021.100156.

(13) Gil Posada, J. O.; Hall, P. J. Post-Hoc Comparisons among Iron Electrode Formulations Based on Bismuth, Bismuth Sulphide, Iron Sulphide, and Potassium Sulphide under Strong Alkaline Conditions. *J Power Sources* **2014**, *268*, 810–815. https://doi.org/10.1016/J.JPOWSOUR.2014.06.126.

(14) Narayanan, S. R.; Prakash, G. K. S.; Manohar, A.; Yang, B.; Malkhandi, S.; Kindler, A. Materials Challenges and Technical Approaches for Realizing Inexpensive and Robust Iron–Air Batteries for Large-Scale Energy Storage. *Solid State Ion* **2012**, *216*, 105–109. https://doi.org/10.1016/J.SSI.2011.12.002.

(15) Chen, Z.; Bian, S.; Chen, W.; Ye, F.; Cheng, C.; Shu, S.; Gu, Q.; Dong, H.; Feng, P.; Wu, Y.; Hu, L. An Air-Operated, High-Performance Fe-Ion Secondary Battery Using Acidic Electrolyte. *Advanced Materials* **2025**. https://doi.org/10.1002/ADMA.202502526.

(16) Vijayamohanan, K.; Balasubramanian, T. S.; Shukla, A. K. Rechargeable Alkaline Iron Electrodes. *J Power Sources* **1991**, *34* (3), 269–285. https://doi.org/10.1016/0378-7753(91)80093-D.

(17) Gimenez-Garcia, I.; Forner-Cuenca, A. Elucidating the Influence of Electrolyte Additives on Iron Electroplating Performance. *Electrochim Acta* **2024**, *498*, 144509. https://doi.org/10.1016/J.ELECTACTA.2024.144509.

(18) Li, Y.; Cui, Z.; Zhang, L.; Yan, B.; Tao, H.; Yang, X. Hydrogen Evolution Inhibition via Dual Functional Electrolyte Additive to Achieve Highly Stable Aqueous Fe Ion Battery. *Adv Funct Mater* **2025**. https://doi.org/10.1002/ADFM.202424582.

(19) Hawthorne, K. L.; Petek, T. J.; Miller, M. A.; Wainright, J. S.; Savinell, R. F. An Investigation into Factors Affecting the Iron Plating Reaction for an All-Iron Flow Battery. *J Electrochem Soc* **2015**, *162* (1), A108–A113. https://doi.org/10.1149/2.0591501JES/XML.

(20) Liu, J.; Dong, D.; Caro, A. L.; Andreas, N. S.; Li, Z.; Qin, Y.; Bedrov, D.; Gao, T. Aqueous Electrolytes Reinforced by Mg and Ca Ions for Highly Reversible Fe Metal Batteries. *ACS Cent Sci* **2022**, *8* (6), 729–740. https://doi.org/10.1021/acscentsci.2c00293.

(21) Greenburg, L. C.; Holoubek, J.; Cui, Y.; Zhang, P.; Ai, H.; Zhang, E.; Liu, C.; Feng, G.; Cui, Y. Crowding Agent Stabilizes Aqueous Electrolyte for Reversible Iron Metal Anode. *ACS Energy Lett* **2025**, 1022–1029. https://doi.org/10.1021/acsenergylett.4c03268.

(22) Li, X.; Liu, P.; Han, C.; Cai, T.; Cui, Y.; Xing, W.; Zhi, C. Corrosion of Metallic Anodes in Aqueous Batteries. *Energy Environ Sci* **2025**. https://doi.org/10.1039/D5EE00075K.

(23) Zhao, Y.; Hu, X.; Stucky, G. D.; Boettcher, S. W. Thermodynamic, Kinetic, and Transport Contributions to Hydrogen Evolution Activity and Electrolyte-Stability Windows for Water-in-Salt Electrolytes. *J Am Chem Soc* **2024**, *146* (5), 3438–3448. https://doi.org/10.1021/JACS.3C12980.

(24) Qiu, H.; Du, X.; Zhao, J.; Wang, Y.; Ju, J.; Chen, Z.; Hu, Z.; Yan, D.; Zhou, X.; Cui, G. Zinc Anode-Compatible in-Situ Solid Electrolyte Interphase via Cation Solvation Modulation. *Nat Commun* **2019**, *10* (1). https://doi.org/10.1038/s41467-019-13436-3.

(25) Wang, D.; Lv, D.; Peng, H.; Wang, C.; Liu, H.; Yang, J.; Qian, Y. Solvation Modulation Enhances Anion-Derived Solid Electrolyte Interphase for Deep Cycling of Aqueous Zinc Metal Batteries. *Angewandte Chemie - International Edition* **2023**, *62* (38). https://doi.org/10.1002/anie.202310290.

(26) Li, H.; Chen, Z.; Zheng, L.; Wang, J.; Adenusi, H.; Passerini, S.; Zhang, H. Electrolyte Strategies Facilitating Anion-Derived Solid-Electrolyte Interphases for Aqueous Zinc–

View Article Online
DOI: 10.1039/D5TA03206G

Metal Batteries. *Small Methods*. John Wiley and Sons Inc June 20, 2024. https://doi.org/10.1002/smtd.202300554.

(27) Bruchiel-Spanier, N.; Blumen, O.; Lahav, L.; Romem, A.; Shwartsman, K.; Chae, M. S.; Bar-Lev, I.; Gross, E.; Shpigel, N.; Sharon, D. Enhancing the Performance of Reversible Zn Deposition by Ultrathin Polyelectrolyte Coatings. *ACS Applied Materials and Interfaces* **2023**, *15* (49), 57699–57707. https://doi.org/10.1021/ACSAMI.3C14663.

(28) Bergman, G.; Bruchiel-Spanier, N.; Bluman, O.; Levi, N.; Harpaz, S.; Malchick, F.; Wu, L.; Sonoo, M.; Chae, M. S.; Wang, G.; Mandler, D.; Aurbach, D.; Zhang, Y.; Shpigel, N.; Sharon, D. To What Extent Do Anions Affect the Electrodeposition of Zn? *J Mater Chem A Mater* **2024**, *12* (24), 14456–14466. https://doi.org/10.1039/D4TA01466A.

(29) Wang, Y.; Cheng, G.; Wu, W.; Qiao, Q.; Li, Y.; Li, X. Effect of PH and Chloride on the Micro-Mechanism of Pitting Corrosion for High Strength Pipeline Steel in Aerated NaCl Solutions. *Appl Surf Sci* **2015**, *349*, 746–756. https://doi.org/10.1016/J.APSUSC.2015.05.053.

(30) Wan, Y.; Tan, J.; Zhu, S.; Cui, J.; Zhang, K.; Wang, X.; Shen, X.; Li, Y.; Zhu, X. Insight into Atmospheric Pitting Corrosion of Carbon Steel via a Dual-Beam FIB/SEM System Associated with High-Resolution TEM. *Corros Sci* **2019**, *152*, 226–233. https://doi.org/10.1016/J.CORSCI.2019.03.017.

(31) Alvarez, M. G.; Galvele, J. R. The Mechanism of Pitting of High Purity Iron in NaCl Solutions. *Corros Sci* **1984**, *24* (1), 27–48. https://doi.org/10.1016/0010-938X(84)90133-1.

(32) Li, Z.; Ganapathy, S.; Xu, Y.; Zhou, Z.; Sarilar, M.; Wagemaker, M. Mechanistic Insight into the Electrochemical Performance of Zn/VO2 Batteries with an Aqueous ZnSO4 Electrolyte. *Adv Energy Mater* **2019**, *9* (22), 1900237. https://doi.org/10.1002/AENM.201900237.

(33) Wang, D.; Zhang, Z.; Hao, Y.; Jia, H.; Shen, X.; Qu, B.; Huang, G.; Zhou, X.; Wang, J.; Xu, C.; Pan, F. Challenges and Progress in Rechargeable Magnesium-Ion Batteries: Materials, Interfaces, and Devices. *Adv Funct Mater* **2024**, 2410406. https://doi.org/10.1002/ADFM.202410406.

(34) Gong, X.; Zhang, Z.; Zhang, Z.; Dai, J.; Li, X.; Wang, B. Insights Into Electrolyte Strategies for Suppressing Side Reactions Towards Aqueous Zinc-Ion Batteries. *Batter Supercaps* **2024**, *7* (6), e202400095. https://doi.org/10.1002/BATT.202400095.

(35) Blumen, O.; Bergman, G.; Schwatrzman, K.; Harpaz, S.; Akella, S. H.; Chae, M. S.; Bruchiel-Spanier, N.; Shpigel, N.; Sharon, D. Selection Criteria for Current Collectors for Highly Efficient Anode-Free Zn Batteries. *J Mater Chem A Mater* **2023**, *11* (37), 19970–19980. https://doi.org/10.1039/D3TA03766E.

(36) Hughes, A. E.; Easton, C. D.; Gengenbach, T. R.; Biesinger, M. C.; Laleh, M. Interpretation of Complex X-Ray Photoelectron Peak Shapes. II. Case Study of Fe 2p3/2 Fitting Applied to Austenitic Stainless Steels 316 and 304. *Journal of Vacuum Science & Technology A* **2024**, *42* (5). https://doi.org/10.1116/6.0003842/3309425.

(37) Biesinger, M. C.; Payne, B. P.; Grosvenor, A. P.; Lau, L. W.; Gerson, A. R.; StC Smart, R. Resolving Surface Chemical States in XPS Analysis of First Row Transition Metals, Oxides

View Article Online
DOI: 10.1039/D5TA03206G

and Hydroxides: Cr, Mn, Fe, Co and Ni. *Appl Surf Sci* **2011**, *257*, 2717–2730. https://doi.org/10.1016/j.apsusc.2010.10.051.

(38) Carlson, T. A.; McGuire, G. E. Study of the X-Ray Photoelectron Spectrum of Tungsten—Tungsten Oxide as a Function of Thickness of the Surface Oxide Layer. *J Electron Spectros Relat Phenomena* **1972**, *1* (2), 161–168. https://doi.org/10.1016/0368-2048(72)80029-X.

(39) Strohmeier, B. R. An ESCA Method for Determining the Oxide Thickness on Aluminum Alloys. *Surface and Interface Analysis* **1990**, *15* (1), 51–56. https://doi.org/10.1002/SIA.740150109.

(40) Biesinger, M. C.; Payne, B. P.; Lau, L. W. M.; Gerson, A.; Smart, R. S. C. X-Ray Photoelectron Spectroscopic Chemical State Quantification of Mixed Nickel Metal, Oxide and Hydroxide Systems. *Surface and Interface Analysis* **2009**, *41* (4), 324–332. https://doi.org/10.1002/SIA.3026.

(41) Biesinger, M. C. Advanced Analysis of Copper X-Ray Photoelectron Spectra. *Surface and Interface Analysis* **2017**, *49* (13), 1325–1334. https://doi.org/10.1002/SIA.6239.

(42) Gai X As, G.; Gai, G.; Silvestri, V. J.; Lyons, V. J. The Anodic Oxidation of Iron in a Neutral Solution: I . The Nature and Composition of the Passive Film. *J Electrochem Soc* **1962**, *109* (9), 781. https://doi.org/10.1149/1.2425555.

(43) Kanie, K.; Muramatsu, A.; Suzuki, S.; Waseda, Y. Influence of Sulfate Ions on Conversion of Fe(OH)3 Gel to β-FeOOH and α-Fe2O3. *Mater Trans* **2004**, *45* (3), 968–971. https://doi.org/10.2320/MATERTRANS.45.968.

(44) Leygraf, Christofer.; Odnevall Wallinder, Inger.; Tidblad, Johan.; Graedel, T. E. . Atmospheric Corrosion. **2016**, 374.

(45) Tamura, H. The Role of Rusts in Corrosion and Corrosion Protection of Iron and Steel. *Corros Sci* **2008**, *50* (7), 1872–1883. https://doi.org/10.1016/J.CORSCI.2008.03.008.

(46) Yamashita, M.; Miyuki, H.; Matsuda, Y.; Nagano, H.; Misawa, T. The Long Term Growth of the Protective Rust Layer Formed on Weathering Steel by Atmospheric Corrosion during a Quarter of a Century. *Corros Sci* **1994**, *36* (2), 283–299. https://doi.org/10.1016/0010-938X(94)90158-9.

(47) Payne, B. P.; Biesinger, M. C.; McIntyre, N. S. X-Ray Photoelectron Spectroscopy Studies of Reactions on Chromium Metal and Chromium Oxide Surfaces. *J Electron Spectros Relat Phenomena* **2011**, *184* (1–2), 29–37. https://doi.org/10.1016/J.ELSPEC.2010.12.001.

(48) Henderson, J. D.; Payne, B. P.; McIntyre, N. S.; Biesinger, M. C. Enhancing Oxygen Spectra Interpretation by Calculating Oxygen Linked to Adventitious Carbon. *Surface and Interface Analysis* **2025**, *57* (3), 214–220. https://doi.org/10.1002/SIA.7376.

(49) Gui, J.; Devine, T. M. The Influence of Sulfate Ions on the Surface Enhanced Raman Spectra of Passive Films Formed on Iron. *Corros Sci* **1994**, *36* (3), 441–462. https://doi.org/10.1016/0010-938X(94)90036-1.

(50) Morgan, D. J. The Utility of Adventitious Carbon for Charge Correction: A Perspective From a Second Multiuser Facility. *Surface and Interface Analysis* **2025**, *57* (1), 28–35. https://doi.org/10.1002/SIA.7360.

(51) Biesinger, M. C. Accessing the Robustness of Adventitious Carbon for Charge Referencing (Correction) Purposes in XPS Analysis: Insights from a Multi-User Facility Data Review. *Appl Surf Sci* **2022**, *597*, 153681. https://doi.org/10.1016/J.APSUSC.2022.153681.

(52) Zhang, X.; Xiao, K.; Dong, C.; Wu, J.; Li, X.; Huang, Y. In Situ Raman Spectroscopy Study of Corrosion Products on the Surface of Carbon Steel in Solution Containing Cl− and SO42-. *Eng Fail Anal* **2011**, *18* (8), 1981–1989. https://doi.org/10.1016/J.ENGFAILANAL.2011.03.007.

(53) Davidson, S.; Berry, J.; Abbott, P.; Xiao, Z.; Tan, C.; Dong, F.; Schelles, M.; Wouters, J.; Asamoah, B.; Vietti, A.; Angelini, E.; Grassini, S.; Donato, N. Raman Spectroscopic Characterization of Corrosion Products of Archaeological Iron. *J Phys Conf Ser* **2022**, *2204* (1), 012066. https://doi.org/10.1088/1742-6596/2204/1/012066.

(54) Ohtsuka, T.; Tanaka, S. Monitoring the Development of Rust Layers on Weathering Steel Using in Situ Raman Spectroscopy under Wet-and-Dry Cyclic Conditions. *Journal of Solid State Electrochemistry* **2015**, *19* (12), 3559–3566. https://doi.org/10.1007/S10008-015-2825-8.

(55) Thinaharan, C.; George, R. P.; Philip, J. In Situ Raman Spectroscopic Analysis on Carbon Steel, Immersed in Aqueous Solutions at Different PH and Anions. *J Mater Eng Perform* **2020**, *29* (5), 2792–2805. https://doi.org/10.1007/S11665-020-04805-X.

(56) Amirudin, A.; Thieny, D. Application of Electrochemical Impedance Spectroscopy to Study the Degradation of Polymer-Coated Metals. *Prog Org Coat* **1995**, *26* (1), 1–28. https://doi.org/10.1016/0300-9440(95)00581-1.

(57) Hernández, H. H.; Reynoso, A. M. R.; González, J. C. T.; Morán, C. O. G.; Hernández, J. G. M.; Ruiz, A. M.; Hernández, J. M.; Cruz, R. O.; Hernández, H. H.; Reynoso, A. M. R.; González, J. C. T.; Morán, C. O. G.; Hernández, J. G. M.; Ruiz, A. M.; Hernández, J. M.; Cruz, R. O. Electrochemical Impedance Spectroscopy (EIS): A Review Study of Basic Aspects of the Corrosion Mechanism Applied to Steels. *Electrochemical Impedance Spectroscopy* **2020**. https://doi.org/10.5772/INTECHOPEN.94470.

(58) Liang, D. D.; Wei, X. S.; Wang, Y.; Jiang, H. R.; Shen, J. Electrochemical Behaviors and Passive Film Properties of Fe-Based Bulk Metallic Glass in Cl−-Containing Acetic Acid Solutions under High Temperature. *J Alloys Compd* **2018**, *766*, 964–972. https://doi.org/10.1016/J.JALLCOM.2018.07.029.

(59) Song, G.; Cao, C. N.; Chen, S. H. A Study on Transition of Iron from Active into Passive State. *Corros Sci* **2005**, *47* (2), 323–339. https://doi.org/10.1016/J.CORSCI.2004.05.027.

(60) Ogunsanya, I. G.; Hansson, C. M. Influence of Chloride and Sulphate Anions on the Electronic and Electrochemical Properties of Passive Films Formed on Steel Reinforcing Bars. *Materialia (Oxf)* **2019**, *8*, 100491. https://doi.org/10.1016/J.MTLA.2019.100491.

(61) McCafferty, E. A Competitive Adsorption Model for the Inhibition of Crevice Corrosion and Pitting. *J Electrochem Soc* **1990**, *137* (12), 3731–3737. https://doi.org/10.1149/1.2086294/XML.

(62) Ashley, G. W.; Burstein, G. T. Initial Stages of the Anodic Oxidation of Iron in Chloride Solutions. *Corrosion* **1991**, *47* (12), 908–916. https://doi.org/10.5006/1.3585204.

(63) Zhang, C.; Holoubek, J.; Wu, X.; Daniyar, A.; Zhu, L.; Chen, C.; Leonard, D. P.; Rodríguez-Pérez, I. A.; Jiang, J. X.; Fang, C.; Ji, X. A ZnCl2 Water-in-Salt Electrolyte for a Reversible Zn Metal Anode. *Chemical Communications* **2018**, *54* (100), 14097–14099. https://doi.org/10.1039/C8CC07730D.

(64) Yang, F.; Yuwono, J. A.; Hao, J.; Long, J.; Yuan, L.; Wang, Y.; Liu, S.; Fan, Y.; Zhao, S.; Davey, K.; Guo, Z.; Yang, F.; Yuwono, J. A.; Hao, J.; Yuan, L.; Wang, Y.; Liu, S.; Zhao, S.; Davey, K.; Guo, Z.; Fan, Y. Understanding H2 Evolution Electrochemistry to Minimize Solvated Water Impact on Zinc-Anode Performance. *Advanced Materials* **2022**, *34* (45), 2206754. https://doi.org/10.1002/ADMA.202206754.

(65) Dong, N.; Zhang, F.; Pan, H. Towards the Practical Application of Zn Metal Anodes for Mild Aqueous Rechargeable Zn Batteries. *Chem Sci* **2022**, *13* (28), 8243–8252. https://doi.org/10.1039/D2SC01818G.

View Article Online
DOI: 10.1039/D5TA03206G

Data availability. All datasets generated or analyzed during the current study are included in the paper and its ESI.